JACS
JOURNAL OF THE AMERICAN CHEMICAL SOCIETY
Article
pubs.acs.org/JACS

Tuning Nanoparticle Structure and Surface Strain for Catalysis Optimization

Sen Zhang,[†] Xu Zhang,[‡] Guangming Jiang,[†] Huiyuan Zhu,[†] Shaojun Guo,[†] Dong Su,[§] Gang Lu,[‡] and Shouheng Sun*,[†]

[†]Department of Chemistry, Brown University, Providence, Rhode Island 02912, United States
[‡]Department of Physics and Astronomy, California State University—Northridge, Northridge, California 91330, United States
[§]Center for Functional Nanomaterials, Brookhaven National Laboratory, Upton, New York 11973, United States

Supporting Information

ABSTRACT: Controlling nanoparticle (NP) surface strain, i.e. compression (or stretch) of surface atoms, is an important approach to tune NP surface chemistry and to optimize NP catalysis for chemical reactions. Here we show that surface Pt strain in the core/shell FePt/Pt NPs with Pt in three atomic layers can be rationally tuned via core structural transition from cubic solid solution [denoted as face centered cubic (fcc)] structure to tetragonal intermetallic [denoted as face centered tetragonal (fct)] structure. The high activity observed from the fct-FePt/Pt NPs for oxygen reduction reaction (ORR) is due to the release of the overcompressed Pt strain by the fct-FePt as suggested by quantum mechanics−molecular mechanics (QM−MM) simulations. The Pt strain effect on ORR can be further optimized when Fe in FePt is partially replaced by Cu. As a result, the fct-FeCuPt/Pt NPs become the most efficient catalyst for ORR and are nearly 10 times more active in specific activity than the commercial Pt catalyst. This structure-induced surface strain control opens up a new path to tune and optimize NP catalysis for ORR and many other chemical reactions.

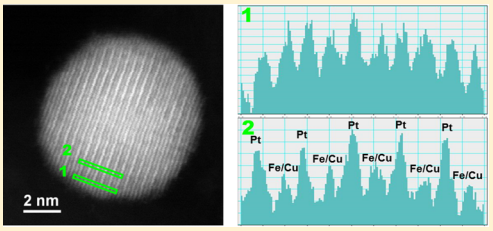

1. INTRODUCTION

In the search for highly efficient nanoparticle (NP) catalysts for chemical conversions, one often explores NPs' sizes, shapes, and compositions as important parameters to tune NPs' catalytic properties.[1−5] It has become increasingly important to rationalize NP parameters with catalysis in order to provide predictable models for catalyst design and optimization.[6−10] NPs based on platinum (Pt) have constantly been the subject of the studies due to their unique properties shown in catalyzing many chemical reactions, including the oxygen reduction reaction (ORR), an important cathodic reaction used in low-temperature polymer electrolyte membrane fuel cells and metal−air batteries.[11−20] Recent studies on ORR have indicated that Pt−Pt bond compression, and the resultant d-band down-shift, weakens the bonding between Pt and oxygenated species (O) and increases catalytic activity for ORR.[21−27] Density functional theory (DFT) calculations further suggest that Pt−O binding energy (E_O), a key "descriptor" to measure the adsorption/desorption of oxygenated species, should be 0.2 eV higher (ΔE_O = 0.2 eV) than the corresponding value on the Pt(111) surface in order for a Pt catalyst to achieve optimal ORR activity.[28−31] An unanswered, yet extremely important, question related to Pt-based ORR catalysis is if indeed there exists a form of Pt NP catalyst whose oxygen binding energy coincides with the optimal ΔE_O value for which ORR catalytic efficiency is maximized.

Here we report a strategy to tune and optimize ORR catalysis of multimetallic core/shell NPs by controlling the crystal structure of the core and surface strain of the shell. In previous studies on ORR catalysis, Pt alloy NPs are the universal choice of the catalyst and are often in chemically disordered solid solution structure. Chemically ordered intermetallic structure is rarely considered as a factor due to the difficulty in obtaining such a structure without sacrificing other NP parameters, such as size, shape, and composition,[32−35] making it impossible to identify the true nature of the catalytic enhancement. We have synthesized monodisperse FePt alloy NPs with controlled sizes and compositions.[36−38] We noticed that when these alloy NPs were deposited on the carbon support, they could withstand high-temperature treatment without showing any sign of aggregation or sintering, and their solid solution structure [often denoted as face centered cubic (fcc) structure] could be converted to tetragonal intermetallic structure [often denoted as face centered tetragonal (fct) structure]. More importantly, electro-anodization of these FePt NPs in 0.1 M $HClO_4$ led to stable core/shell FePt/Pt NPs with Pt only in about three atomic layers. The fct-core/shell catalyst showed much enhanced catalytic efficiency for ORR, and this enhancement was attributed to more favored release of Pt strain in the fct-FePt/Pt than in the fcc-FePt/Pt, as calculated by the quantum mechanics−molecular mechanics (QM-MM) simulations. The

Received: March 25, 2014
Published: May 6, 2014

dx.doi.org/10.1021/ja5030172 | J. Am. Chem. Soc. 2014, 136, 7734−7739

simulations also suggested that by partially replacing Fe with Cu and forming fct-FeCuPt/Pt NPs, the overcompressed strain in Pt shell could be further released with ΔE_O reaching 0.22 eV, very close to the predicted optimal value at 0.20 eV. Experimentally, the fct-FeCuPt/Pt NPs were indeed the most efficient catalyst for ORR, and their specific activity was nearly 10 times higher than that of the commercial Pt catalyst (Fuel Cells Store).

2. EXPERIMENTAL SECTION

2.1. Chemicals and Materials. Oleylamine (>70%), oleic acid, 1-octadecene, $Pt(acac)_2$ (acac = aceylacetonate), $Cu(acac)_2$, iron pentacarbonyl [$Fe(CO)_5$], hexane, 2-propanol, ethanol, and Nafion (5%) were all purchased from Sigma-Aldrich and used without further purification. The commercial Pt (20% mass loading on carbon with a diameter of 2.5−3.5 nm) catalyst was obtained from Fuel Cell Store.

2.2. Synthesis of FePt NPs. Under a gentle flow of N_2, 1-octadecene (10 mL), oleic acid (1.28 mL, 4 mmol), oleylamine (1.36 mL, 4 mmol), and $Pt(acac)_2$ (0.2 g, 0.5 mmol) were mixed in a four-necked flask. The mixture was magnetically stirred and heated to 120 °C to generate a light yellow solution. Under a N_2 blanket, 0.16 mL (1.23 mmol) of $Fe(CO)_5$ was added into the solution. The solution was heated to 220 °C at a rate of about 3 °C/min and kept at this temperature for 1 h before it was cooled to room temperature. The NPs were separated by adding 2-propanol (50 mL), followed by centrifugation (8500 rpm, 8 min). The NPs were further purified by dispersing into hexane (20 mL) and centrifugation (5000 rpm, 8 min) to remove any undispersed precipitates. The product was precipitated out by adding ethanol (50 mL), the mixture was centrifuged (8500 rpm, 8 min), and the product was redispersed in hexane. The synthesis yielded $Fe_{51}Pt_{49}$ NPs.

Under the same condition and when 1.07 mmol of $Fe(CO)_5$ was used in the synthesis, $Fe_{42}Pt_{58}$ NPs were obtained. In the presence of 1.07 mmol of $Fe(CO)_5$ and at 200 °C (or 180 °C), $Fe_{33}Pt_{67}$ (or $Fe_{27}Pt_{73}$) NPs were separated.

2.3. Synthesis of FeCuPt NPs. FeCuPt NPs were prepared by a seed mediated growth of Cu over FePt NPs followed by Cu diffusion into FePt. In a typical synthesis, 1-octadecene (15 mL), oleylamine (2 mL), and $Cu(acac)_2$ (14 mg) were mixed in a four-necked flask. The mixture was magnetically stirred and heated to 80 °C to generate a bluish green solution under a gentle flow of N_2. Then 40 mg of $Fe_{42}Pt_{58}$ NPs (hexane dispersion) was added into the solution. Upon the evaporation of hexane, the solution was heated to 240 °C at a rate of about 3 °C/min and kept at this temperature for 1 h before it was cooled to room temperature. The NPs were separated by adding 2-propanol (50 mL), followed by centrifugation (8500 rpm, 8 min). The NPs were further purified by dispersing into hexane (20 mL) and centrifugation (5000 rpm, 3 min) to remove any undispersed precipitates. The product was precipitated out by adding ethanol (50 mL), the mixture was centrifuged (8500 rpm, 8 min), and the product eas redispersed in hexane. The synthesis yielded $Fe_{38}Cu_{15}Pt_{47}$ NPs.

Under the same reaction condition, 18 mg of $Cu(acac)_2$ and 40 mg of $Fe_{34}Pt_{66}$ seeds led to the formation of $Fe_{25}Cu_{23}Pt_{52}$ NPs. 24 mg of $Cu(acac)_2$ and 40 mg of $Fe_{27}Pt_{73}$ seeds yielded $Fe_{19}Cu_{35}Pt_{46}$ NPs.

2.4. Catalyst Preparation and NP Structural Control. The as-synthesized NPs and Ketjen-300 J carbon at a weight ratio of 1:2 were mixed in 20 mL of hexane and sonicated for 1 h to deposit NPs on carbon (C−NPs). The product was separated by centrifugation (8500 rpm, 3 min). The C−NPs were dried under ambient conditions and annealed at different temperatures for 1 h in a gas flow of Ar + 5% H_2 to control the NPs structures. The product was then resuspended in a mixture of deionized water, 2-propanol, and Nafion (v/v/v = 4/1/0.05). Twenty microliters of catalyst ink (2 mg/mL) was deposited on the working electrode (glassy carbon rotating disk electrode, GC-RDE) that was polished prior to catalyst deposition by 0.1 and 0.05 μm alumina powder and rinsed by sonication in ethanol and in deionized water. The catalyst was dried in ambient condition.

2.5. Characterizations. X-ray diffraction (XRD) patterns of the NPs were collected on a Bruker AXS D8-Advanced diffractometer with Cu Kα radiation (λ = 1.5418 Å). Transmission electron microscopy (TEM) images were acquired from a Philips CM 20 operating at 200 kV. Scanning transmission electron microscopy (STEM) analyses were carried out on a Hitachi HD2700C (200 kV) with a probe aberration corrector, at the Center for Functional Nanomaterials, Brookhaven National Lab. The electron energy loss spectroscopy (EELS) line-scan was obtained by a high-resolution Gatan-Enfina ER with a probe size of 1.3 Å. A power law function was used for EELS background subtraction. TEM and high-resolution TEM (HRTEM) samples were prepared by depositing a single drop of diluted NPs dispersion on amorphous carbon-coated copper grids. The inductively coupled plasma-atomic emission spectroscopy (ICP-AES) measurements were carried on a JY2000 Ultrace ICP atomic emission spectrometer equipped with a JY AS 421 autosampler and 2400g/mm holographic grating. Electrochemical measurements were performed on an Autolab 302 potentiostat with glassy carbon rotating disk (5 mm in diameter) as a working electrode, Ag/AgCl (4 M KCl) as a reference electrode, and platinum wire as a counter electrode.

2.6. Electrochemical Measurements. The NPs were first subject to cyclic voltammetry (CV) scans between −0.2 and 1.0 V (vs Ag/AgCl) at 100 mV/s in N_2-saturated 0.1 M $HClO_4$ until a stable CV was obtained (150 scans for the fcc-FePt and 300 scans for the fct-FePt NPs). Once the core/shell FePt/Pt NPs were obtained, their CVs were recorded at a scan rate of 50 mV/s in N_2-saturated 0.1 M $HClO_4$ and were used to estimate electrochemically active surface area (ECASA). ORR polarization curves were recorded by linear-sweep voltammetry (LSV) at a scan rate of 10 mV/s in O_2-saturated 0.1 M $HClO_4$ with the GC-RDE rotating at 1600 rpm.

2.7. QM−MM Simulations. Core/shell NPs are modeled by 8 nm cuboctahedrons with eight (111) facets and six (100) facets. The NP consists of an fcc-Pt shell (with three atomic layers) and a FePt or FeCuPt core. ΔE_O relative to the flat Pt(111) surface is determined by placing an O atom at the hollow site on the (111) facet of fcc-Pt, following

$$\Delta E_O = (E_{QM/MM}[NP + O] - E_{QM/MM}[NP]) - (E_{QM}[Pt(111) + O] - E_{QM}[Pt(111)])$$

where $E_{QM/MM}$[NP+O] and $E_{QM/MM}$[NP] are total energies of NPs with and without O adsorbate, respectively, from QM−MM calculations. E_{QM}[Pt(111)+O] and E_{QM}[Pt(111)] are the total energies of the flat Pt(111) surface with and without the absorbed O atom calculated by DFT. The QM−MM simulation details are provided in the Supporting Information (Text S1).

2.8. Equilibrium Lattice Constants of FePt and FeCuPt from DFT Calculations. A periodic supercell consisting of 108 atoms is used to determine the atomic structure of FePt or FeCuPt cores. For fcc-Fe(Cu)Pt, Pt and Fe(Cu) atoms are randomly arranged in the supercell. For fct-Fe(Cu)Pt, alternating Pt and Fe(Cu) layers are arranged in the supercell. Fe and Cu atoms are randomly arranged in the Fe (Cu) atom layers. All atoms are fully relaxed under constant zero pressure by using the DFT calculations, and details are provided in the Supporting Information (Text S2).

3. RESULTS AND DISCUSSION

The fcc-FePt NPs were synthesized by the reduction of platinum acetylacetonate, $Pt(acac)_2$, and thermal decomposition of iron pentacarbonyl, $Fe(CO)_5$, in the presence of oleylamine and oleic acid as reported.[38] This simple mixing and heating approach led to the formation of monodisperse FePt NPs with a high yield (≥97% based on Pt) and could be scaled-up for mass production. Fe/Pt compositions were controlled by $Fe(CO)_5/Pt(acac)_2$ molar ratios and reaction temperatures and were analyzed by inductively coupled plasma-atomic emission spectroscopy (ICP-AES). Transmission electron microscopy (TEM) images show that the as-synthesized fcc-$Fe_{51}Pt_{49}$ NPs

dx.doi.org/10.1021/ja5030172 | J. Am. Chem. Soc. 2014, 136, 7734−7739

are cubelike with lateral dimension of 8.5 ± 0.5 nm (Figure 1a; TEM images of the other Pt-rich FePt NPs of similar sizes are

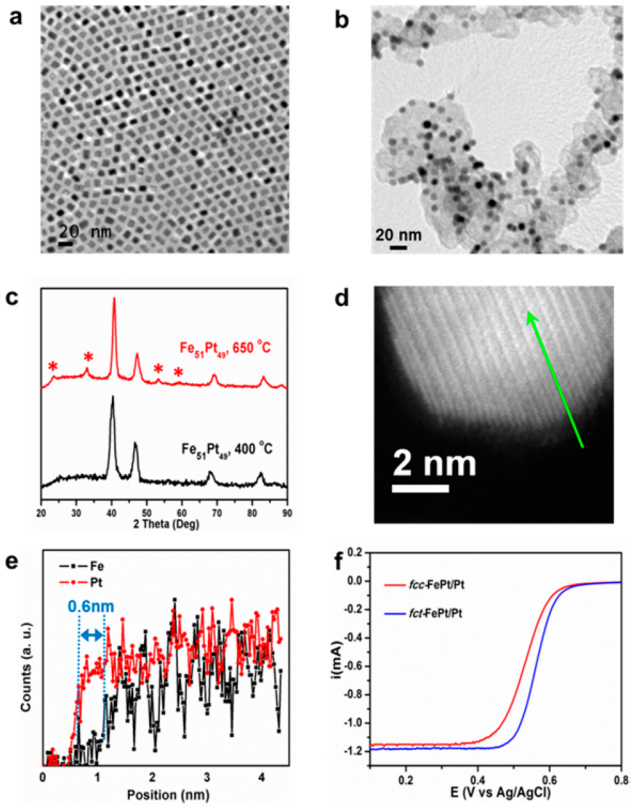

Figure 1. (a, b) TEM images of the as-synthesized fcc-$Fe_{51}Pt_{49}$ NPs (a) and the C−$Fe_{51}Pt_{49}$ NPs annealed at 650 °C (b). (c) XRD patterns of the C−$Fe_{51}Pt_{49}$ NPs annealed at 400 and 650 °C (stars denote the typical peaks characteristic of fct-FePt). (d, e) HAADF-STEM image (d) and STEM-EELS line scan (e) of an electrochemically dealloyed C−fct-$Fe_{51}Pt_{49}$ NP, forming C−fct-FePt/Pt. The arrow indicates the line scan position. (f) ORR polarization curves of the fcc- and fct-FePt/Pt. The ORR polarization curves were obtained in O_2-saturated 0.1 M $HClO_4$ with the working disk electrode rotating at 1600 rpm and a potential scan rate at 10 mV/s.

shown in Figure S1a−c, of the Supporting Information). The fcc-FePt NPs were deposited on Ketjen carbon (C), similar to what has been reported,[39] and are denoted as C−FePt NPs. The C−FePt NPs were annealed in 95% Ar + 5% H_2 for 1 h at temperatures from 400 to 700 °C, and 650 °C was found to be the optimum temperature to convert fcc-$Fe_{51}Pt_{49}$ to fct-$Fe_{51}Pt_{49}$ without causing obvious NP aggregation/sintering, as shown in Figures 1b,c and Figure S2 (Supporting Information) (other Pt-rich FePt NPs could not be converted into the fct structure under this annealing condition). After annealing, both fcc- and fct-FePt NPs adopted the same thermodynamically more stable polyhedral shape.

The C−fcc-$Fe_{51}Pt_{49}$ (preannealed at 400 °C) and C−fct-$Fe_{51}Pt_{49}$ NPs were deposited on GC-RDE and were subject to a potential scan between −0.2 and 1.0 V (vs Ag/AgCl) in the N_2-saturated 0.1 M $HClO_4$ solution until a stable current−potential curve was obtained. The process oxidized and dissolved the surface Fe, leading to the formation of stable core/shell FePt/Pt NPs. The core/shell structure was characterized by aberration-corrected high-angle annular dark field scanning transmission electron microscopy (HAADF-STEM) and STEM-electron energy loss spectroscopy (STEM-EELS), as shown in Figures 1d,e and S3 (Supporting Information). Both the fcc- and fct-$Fe_{51}Pt_{49}$ NPs show a Pt shell of ∼0.6 nm (ca. three atomic layers) with the FePt cores maintaining their structures. In addition, the alternate Pt and Fe layers in the fct-FePt core region are clearly indicated by their brighter (high Z contrast for Pt) and darker (low Z contrast for Fe) contrasts.[40] In the core/shell NPs, the Fe/Pt composition is stabilized at 25/75 in the fcc-FePt/Pt and 26/74 in the fct-FePt/Pt, indicating that the core/shell NPs have the same Fe/Pt ratios.

The electrochemically active surface area (ECASA) of the FePt/Pt, as well as the commercial Pt (2.5−3.5 nm Pt NPs; Figure S4, Supporting Information), were obtained by integrating the hydrogen underpotential desorption (H_{upd}) peaks of their cyclic voltammograms (CVs) (Figure S5, Supporting Information).[41] Their ORR polarization curves are shown in Figure 1f with the half-wave potentials ($E_{1/2}$) at 0.562 V (for the fct-FePt/Pt) and 0.533 V (for the fcc-FePt/Pt). As a comparison, the $E_{1/2}$ of the commercial Pt is at 0.531 V, at which the core/shell NPs have a specific activity of 2.1 mA/cm^2 (for the fct-FePt/Pt) and 0.89 mA/cm^2 (for the fcc-FePt/Pt).

Since both fcc-FePt/Pt and fct-FePt/Pt are monodisperse NPs with the same size, shape, Fe/Pt ratio, and Pt thickness (ca. three atomic layers of Pt), their ORR catalysis difference must originate from structure-induced surface change. To understand this change, we performed QM−MM simulations to calculate Pt−O binding energies on the surface of the FePt/Pt NPs (Supporting Information). The QM−MM modeling combines both the quantum mechanical and classical descriptions, where the QM density functional theory (DFT) is applied to reactive sites to capture chemical reactions, while the long-range strain field of NPs is handled by the classical MM method.[42,43] As a result, the QM−MM method can treat much larger particle sizes (e.g., 8 nm) than previously feasible (∼1 nm).[44,45] We built an 8 nm cuboctahedral core/shell NP model consisting of $Fe_{50}Pt_{50}$ alloy core (fcc- or fct-FePt) and fcc-Pt shell (three atomic layers) (Figure 2a,b). The core/shell FePt/Pt NPs have a theoretical composition of around $Fe_{25}Pt_{75}$, consistent with the FePt/Pt NPs studied experimentally. Figure 2c illustrates atomic configuration of a cuboctahedral NP, which is partitioned to the QM region and MM region. By using QM−MM and by placing an O atom at the center of the QM region, we calculated ΔE_O values of the fcc-FePt/Pt and fct-FePt/Pt to be 0.26 and 0.23 eV, respectively. Commercial Pt catalyst was also simulated to have a ΔE_O of 0.1 eV based on the QM−MM method and the 3 nm NP model, which was consistent with the previous reported value through DFT calculations.[30] We can easily expect that a NP catalyst more active than commercial Pt NP should possess a ΔE_O in the range of 0.1−0.3 eV (0.2 eV is the optimal value). Our fcc-FePt/Pt and fct-FePt/Pt fall into this regime. As the ΔE_O value of the fct-FePt/Pt is closer to the optimal value of 0.20 eV, the fct-FePt/Pt shows higher ORR activity than the fcc-FePt/Pt.

ΔE_O is related to the compression (or stretch) of Pt (i.e., Pt strain) on the catalyst surface.[21] In our FePt/Pt core/shell structure this strain is caused by the crystal lattice mismatch between the core and the shell. Using the supercell models (Figure 2d,e and Supporting Information) and DFT, we calculated the equilibrium crystalline lattice constants (Table S1, Supporting Information) and the surface Pt strain (ε) of the fcc- and fct-FePt/Pt and compared them with fcc-Pt (Table 1).

dx.doi.org/10.1021/ja5030172 | J. Am. Chem. Soc. 2014, 136, 7734−7739

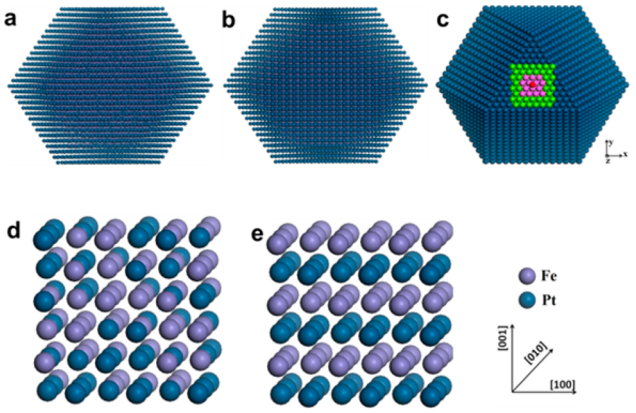

Figure 2. (a, b) Eight nanometer cuboctahedral fcc-FePt/Pt (a) and fct-FePt/Pt (b) core/shell models constructed for QM−MM calculations. Model a contains 7667 Pt atoms and 2512 Fe atoms, and model b consists of 7704 Pt atoms and 2405 Fe atoms. Both models have a core composition of $Fe_{50}Pt_{50}$ and a shell of three-atomic-layer Pt. (c) Atomic configuration of a cuboctahedron NP for QM−MM calculation, viewing along the ⟨111⟩ direction. The entire system is partitioned into a QM region (red, pink, and green spheres) and a MM region (blue spheres). The red sphere represents the adsorbed O atom. (d, e) The periodic supercells of fcc-$Fe_{50}Pt_{50}$ (d) and fct-$Fe_{50}Pt_{50}$ (e) used to calculate the crystalline lattice constants.

Table 1. Surface Strain (ε, in %) from DFT Calculations and ΔE_O from QM−MM Simulations

catalyst	$\varepsilon_{[100]}$	$\varepsilon_{[010]}$	$\varepsilon_{[001]}$	ΔE_O (eV)
fcc-FePt/Pt	3.9	3.6	3.5	0.26
fct-FePt/Pt	2.9	2.9	5.5	0.23
fcc-FeCuPt/Pt	3.3	3.7	3.3	0.25
fct-FeCuPt/Pt	1.4	1.5	5.0	0.22
ideal Pt		2.3		0.20

Compressive strain is calculated by $\varepsilon_i = (a_{Pt} - a_i)/a_{Pt}$, where i indicates [100], [010], and [001] directions. a_{Pt} is the lattice constant of fcc-Pt, and a_i is the interplanar distance along the i direction of each core material.

Both fcc- and fct-FePt have smaller lattice constants than Pt, and the corresponding surface Pt strains are 3%−5%, higher than the 2.3% required for the optimal ΔE_O (0.20 eV).[22] When the fcc-FePt serves as a core, the surface Pt is slightly overcompressed (ΔE_O = 0.26 eV). But when fcc-FePt transforms to fct-FePt in the core, the interplanar distance of the core expands in the [100]/[010] directions and shrinks in the [001] direction. The overall effect is to relieve the overcompression on the Pt surface, resulting in a better ΔE_O and higher activity for ORR.

To further improve ΔE_O by releasing the overcompression on the Pt shell, the fct core structure should be expanded. Our DFT calculations show that when Fe atoms are substituted partially by Cu atoms, the lattice constant can be increased (Table S1, Supporting Information). With the similar core/shell structures, our theoretical models illustrated in Figure 2a,b can be readily extended to FeCuPt (Figure S6, Supporting Information) with the core composition of $Fe_{25}Cu_{25}Pt_{50}$. The QM−MM simulations on FeCuPt/Pt demonstrated that the Cu substitution in FePt could further reduce the overcompression on the Pt shell (Table 1). As a result, ΔE_O of the fct-FeCuPt/Pt was reduced to 0.22 eV, being the closest to the optimal value in our studied four core/shell NPs. This optimized ΔEo is predicted to give the fct-FeCuPt/Pt the balanced energetics for the adsorption and desorption of oxygenated intermediates, which could further enhance the ORR catalytic performance.

To prove experimentally the effect of Cu on Pt strain release and ORR catalysis enhancement, we synthesized fcc-FeCuPt NPs by reacting FePt NPs with $Cu(acac)_2$ and oleylamine in 1-octadecene at 240 °C to facilitate $Cu(acac)_2$ reduction and Cu diffusion into FePt NPs. The Cu content was controlled by FePt/$Cu(acac)_2$ ratios and $Fe_{38}Cu_{15}Pt_{47}$, $Fe_{25}Cu_{23}Pt_{52}$, and $Fe_{19}Cu_{35}Pt_{46}$ NPs were synthesized. TEM images show that the FeCuPt NPs have size (8.5 ± 0.5 nm for $Fe_{38}Cu_{15}Pt_{47}$, 8.6 ± 0.5 nm for $Fe_{25}Cu_{23}Pt_{52}$, and 8.8 ± 0.6 nm for $Fe_{19}Cu_{35}Pt_{46}$) and morphology (cubelike) similar to those of the FePt NPs (Figure 3a−c). Once supported on C and annealed, these

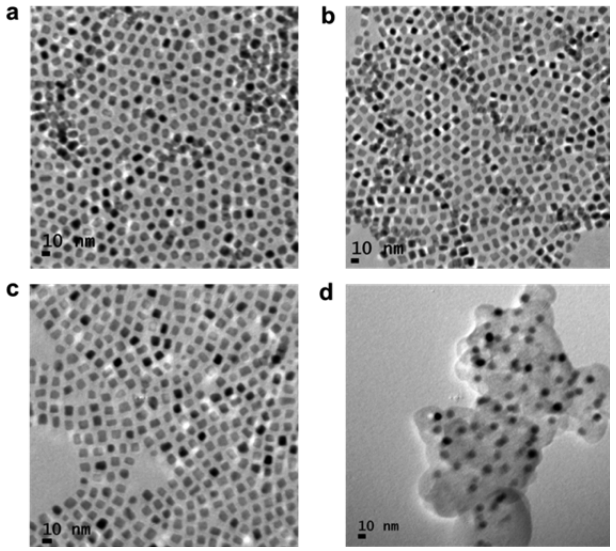

Figure 3. TEM images of the as-synthesized (a) $Fe_{38}Cu_{15}Pt_{47}$, (b) $Fe_{25}Cu_{23}Pt_{52}$, (c) $Fe_{19}Cu_{35}Pt_{46}$ NPs, and (d) the C−fct-$Fe_{25}Cu_{23}Pt_{52}$ NPs made from annealing of fcc-$Fe_{25}Cu_{23}Pt_{52}$ NPs at 650 °C.

FeCuPt NPs were well-dispersed on C (Figure 3d) and showed a Cu-dependent fcc−fct transition (Figure 4). At 400 °C, all FeCuPt are still fcc NPs, showing the homogeneous trimetallic

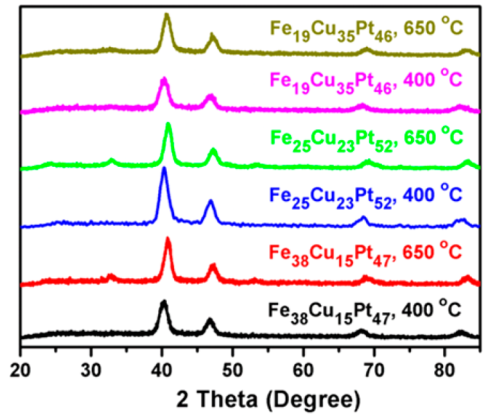

Figure 4. XRD patterns of the $Fe_{38}Cu_{15}Pt_{47}$, $Fe_{25}Cu_{23}Pt_{52}$, and $Fe_{19}Cu_{35}Pt_{46}$ NPs annealed at 400 and 650 °C. The NPs were first deposited on the Ketjen carbon support and then annealed under 95% Ar + 5% H_2 for 1 h.

dx.doi.org/10.1021/ja5030172 | J. Am. Chem. Soc. 2014, 136, 7734−7739

solid solution structures (Figure 5a). At 650 °C, both $Fe_{38}Cu_{15}Pt_{47}$ and $Fe_{25}Cu_{23}Pt_{52}$ NPs showed better fcc–fct

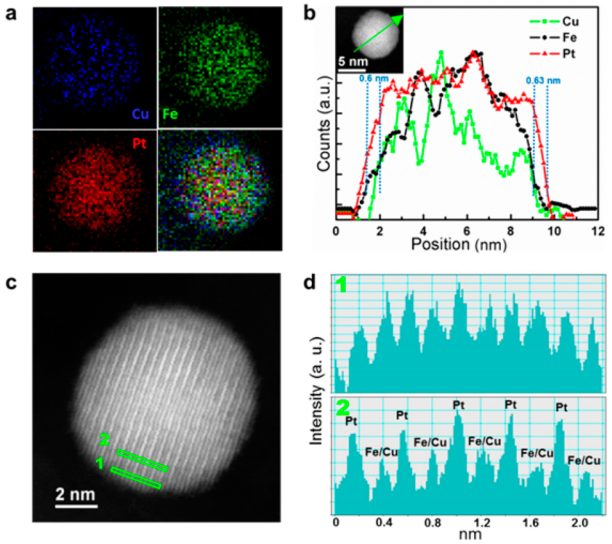

Figure 5. (a) 2D EELS elemental mapping of Fe, Cu and Pt of a fcc-$Fe_{25}Cu_{23}Pt_{52}$ NP annealed at 400 °C, showing a solid solution structure. (b) STEM-EELS line scan crossing a fct-FeCuPt/Pt (dealloyed from fct-$Fe_{25}Cu_{23}Pt_{52}$) NP. The inset shows the NP scanned. (c) HAADF-STEM image of a representative fct-FeCuPt/Pt NP with the indication of two line profiles from the shell and core region. (d) Corresponding HAADF line profile shown in (c) normalized with Z contrast of metal atoms.

transition than the $Fe_{19}Cu_{35}Pt_{46}$ NPs, indicating that the presence of too much Cu prevents the formation of the fct structure, which is consistent with what has been reported in the thin film studies.[46−49] The $Fe_{25}Cu_{23}Pt_{52}$ NPs were found to show the best ORR activity in the current study and were chosen as a representative catalyst to study the effect of Cu on Pt strain and ORR catalysis.

Similar to the $Fe_{51}Pt_{49}$ NPs, the fcc- and fct-$Fe_{25}Cu_{23}Pt_{52}$ NPs could also be converted into the core/shell FeCuPt/Pt with the Pt shell being ~0.6 nm (ca. three atomic layers) thick, as indicated by STEM-EELS line scans of the FeCuPt/Pt structure (Figures 5b and S7, Supporting Information). The intermetallic structure, represented by the periodic contrast change in the core region of the fct-FeCuPt/Pt, is clearly visible in the HAADF-STEM image (Figure 5c). HAADF-STEM line scans normalized with Z contrast of different atoms in two different regions on the fct-FeCuPt/Pt NP show the characteristic single-component Pt shell and intermetallic fct-FeCuPt core (Figure 5d).

Upon comparing the CVs and ORR polarization curves of the FePt/Pt with those of the FeCuPt/Pt NPs obtained under the same detection conditions (Figures 6a and S8, Supporting Information), we can see that the ORR curves of the FeCuPt NPs are more positively shifted than those of the FePt NPs. The $E_{1/2}$ of the fct-FeCuPt/Pt NPs is at 0.574 V, higher than that of the fct-FePt/Pt NPs at 0.562 V and commercial Pt catalyst at 0.531 V. The fct-FeCuPt/Pt NPs have the specific activity of 2.55 mA/cm^2 at 0.531 V, higher than that of fct-FePt/Pt (2.10 mA/cm^2) (Figure 6b) and almost 10 times higher than that of Pt (0.264 mA/cm^2 at 0.531 V). The fct-FeCuPt/Pt NPs are also extremely durable under the ORR reaction conditions. After 10 000 sweeps between 0.4 and 0.7 V

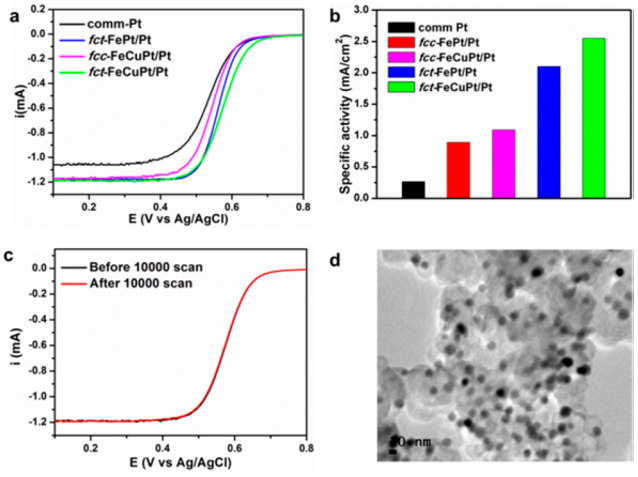

Figure 6. (a) ORR polarization curves of Pt, fct-FePt/Pt, fcc-FeCuPt/Pt, and fct-FeCuPt/Pt NPs. (b) The specific activities of the NP catalysts at 0.531 V ($E_{1/2}$ of the commercial Pt catalyst). (c) ORR polarization curves of the fct-FeCuPt/Pt NPs before and after 10 000 potential scans between 0.4 and 0.7 V. (d) TEM image of the fct-FeCuPt/Pt NPs after 10 000 potential scans.

in the O_2-saturated 0.1 M $HClO_4$, we observed no obvious shift in ORR polarization curves (Figure 6c) and no visible morphology change of NPs (Figure 6d). The fct-FeCuPt/Pt NPs show the best ORR catalytic performance in our experiment, which confirms our theoretical prediction that Cu substitution can further release the Pt surface strain and indeed enhance the catalytic efficiency of the core/shell NPs for ORR.

4. CONCLUSION

The new strategy presented here in tuning Pt shell strain by controlling the FePt structure is a highly efficient way to enhance core/shell FePt/Pt NP catalysis. The FePt/Pt NPs are synthesized by electro-anodization of the FePt alloy NPs. The core FePt structure is controlled to be fcc or fct and the Pt shell is in ca. three atomic layers. The fct-FePt/Pt NPs show much higher activity for ORR than the fcc ones, and the QM–MM simulations reveal that this activity enhancement is due to the release of overcompressed Pt strain and to the improvement of Pt–O binding energy. Our simulations also suggest that the overcompressed strain observed in FePt/Pt can be further released when Fe in the FePt structure is partially replaced by Cu, and the ΔE_O of fct-FeCuPt/Pt can reach 0.22 eV, which is the closest to the optimal 0.20 eV predicted on a Pt surface. Experimentally, fct-FeCuPt/Pt NPs are indeed the most efficient ORR catalyst, showing nearly 10 times higher specific activity than the benchmark Pt catalyst. Our report offers concrete evidence that surface strain in a core/shell NP can be readily tuned by the core structure to achieve catalytic optimization. The strategy presented here is not limited to FePt/Pt NPs but can be extended to other core/shell NPs as well, providing a novel approach to rational tuning of NP catalytic efficiency for many chemical reactions.

■ ASSOCIATED CONTENT

Supporting Information

Texts S1 and S2, giving the details of QM-MM simulations and DFT calculations; Table S1, providing the DFT-calculated crystalline lattice constants of all FePt and FeCuPt cores;

dx.doi.org/10.1021/ja5030172 | J. Am. Chem. Soc. 2014, 136, 7734−7739

Figure S1−S8, giving additional TEM images, HAADF-STEM images, STEM-EELS line scans, CVs, and theoretic models; and Reference S1−S10 for Texts S1 and S2. This material is available free of charge via the Internet at http://pubs.acs.org.

AUTHOR INFORMATION

Corresponding Author

ssun@brown.edu

Notes

The authors declare no competing financial interest.

ACKNOWLEDGMENTS

This work was supported by the U.S. Army Research Laboratory and the U.S. Army Research Office under the Multi University Research Initiative (MURI, grant number W911NF-11-1-0353) on "Stress-Controlled Catalysis via Engineered Nanostructures". Electron microscopy work carried out at the Center for Functional Nanomaterials, Brookhaven National Laboratory, was supported by the U.S. Department of Energy, Office of Basic Energy Sciences, under Contract No. DE-AC02-98CH10886.

REFERENCES

(1) Guo, S.; Zhang, S.; Sun, S. *Angew. Chem., Int. Ed.* **2013**, *52*, 8526−8554.
(2) Yu, W.; Porosoff, M. D.; Chen, J. G. *Chem. Rev.* **2012**, *112*, 5780−5817.
(3) Wang, C.; Daimon, H.; Onodera, T.; Koda, T.; Sun, S. *Angew. Chem., Int. Ed.* **2008**, *47*, 3588−3591.
(4) Tian, N.; Zhou, Z. Y.; Sun, S. G.; Ding, Y.; Wang, Z. L. *Science* **2007**, *316*, 732−735.
(5) Zhu, H.; Zhang, S.; Guo, S.; Su, D.; Sun, S. *J. Am. Chem. Soc.* **2013**, *135*, 7130−7133.
(6) Zhu, H.; Zhang, S.; Huang, Y. X.; Wu, L.; Sun, S. *Nano Lett.* **2013**, *13*, 2947−2951.
(7) Stamenkovic, V. R.; Mun, B. S.; Arenz, M.; Mayrhofer, K. J. J.; Lucas, C. A.; Wang, G.; Ross, P. N.; Markovic, N. M. *Nat. Mater.* **2007**, *6*, 241−247.
(8) Cargnello, M.; Doan-Nguyen, V. V. T.; Gordon, T. R.; Diaz, R. E.; Stach, E. A.; Gorte, R. J.; Fornasiero, P.; Murray, C. B. *Science* **2013**, *341*, 771−773.
(9) Stamenkovic, V. R.; Fowler, B.; Mun, B. S.; Wang, G.; Ross, P. N.; Lucas, C. A.; Markovic, N. M. *Science* **2007**, *315*, 493−497.
(10) Tedsree, K.; Li, T.; Jones, S.; Chan, C. W. A.; Yu, K. M. K.; Bagot, P. A. J.; Marquis, E. A.; Smith, G. D. W.; Tsang, S. C. E. *Nat. Nanotechnol.* **2011**, *6*, 302−307.
(11) Lim, B.; Jiang, M.; Camargo, P. H. C.; Cho, E. C.; Tao, J.; Lu, X.; Zhu, Y.; Xia, Y. *Science* **2009**, *324*, 1302−1305.
(12) Zhang, J.; Mo, Y.; Vukmirovic, M. B.; Klie, R.; Sasaki, K.; Adzic, R. R. *J. Phys. Chem. B* **2004**, *108*, 10955−10964.
(13) Snyder, J.; Fujita, T.; Chen, M. W.; Erlebacher, J. *Nat. Mater.* **2010**, *9*, 904−907.
(14) Zhang, J.; Yang, H.; Fang, J.; Zou, S. *Nano Lett.* **2010**, *10*, 638−644.
(15) Wang, C.; Chi, M.; Li, D.; Strmcnik, D.; Vliet, D. V. D; Wang, G.; Komanicky, V.; Chang, K. C.; Paulikas, A. P.; Tripkovic, D.; Pearson, J.; More, K. L.; Markovic, N. M.; Stamenkovic, V. R. *J. Am. Chem. Soc.* **2011**, *133*, 14396−14403.
(16) Zhang, J.; Sasaki, K.; Sutter, E.; Adzic, R. R. *Science* **2007**, *315*, 220−222.
(17) Cui, C.; Gan, L.; Heggen, M.; Rudi, S.; Strasser, P. *Nat. Mater.* **2013**, *12*, 765−771.
(18) Lu, Y. C.; Xu, Z.; Gasteiger, H. A.; Chen, S.; Hamad-Schifferli, K.; Yang, S. H. *J. Am. Chem. Soc.* **2010**, *132*, 12170−12171.
(19) Cui, C.; Yu, S.-H. *Acc. Chem. Res.* **2013**, *46*, 1427−1437.
(20) Cui, C.; Li, H.-H.; Liu, X.-J.; Gao, M.-R.; Yu, S.-H. *ACS Catal.* **2012**, *2*, 916−924.
(21) Mavrikakis, M.; Hammer, B.; Norskov, J. K. *Phys. Rev. Lett.* **1998**, *81*, 2819−2822.
(22) Nilsson, A.; Pettersson, L. G. M.; Norskov, J. K. *Chemical Bonding at Surfaces and Interfaces*. Elsevier: Amsterdam, 2008.
(23) Adzic, R. R.; Zhang, J.; Sasaki, K.; Vukmirovic, M. B.; Shao, M.; Wang, J. X.; Nilekar, A. U.; Mavrikakis, M.; Uribe, F. *Top. Catal.* **2007**, *46*, 249−262.
(24) Yang, R.; Leisch, J.; Strasser, P.; Toney, M. F. *Chem. Mater.* **2010**, *22*, 4712−4720.
(25) Strasser, P.; Koh, S.; Anniyev, T.; Greeley, J.; More, K. L.; Yu, C.; Liu, Z.; Kaya, S.; Nordlund, D.; Ogasawara, H.; Toney, M. F.; Nilsson, A. *Nat. Chem.* **2010**, *2*, 454−460.
(26) Yang, J.; Yang, J.; Ying, J. Y. *ACS Nano* **2012**, *6*, 9373−9382.
(27) Wu, J.; Qi, L.; You, H.; Gross, A.; Li, J.; Yang, H. *J. Am. Chem. Soc.* **2012**, *134*, 11880−11883.
(28) Norskov, J. K.; Rossmeisl, J.; Logadottir, A.; Lindqvist, L.; Kitchin, J. R.; Bligaard, T.; Jonsson, H. *J. Phys. Chem. B* **2004**, *108*, 17886−17892.
(29) Stamenkovic, V. R.; Mun, B. S.; Mayrhofer, K. J. J.; Ross, P. N.; Markovic, N. M.; Rossmeisl, J.; Greeley, J.; Nørskov, J. K. *Angew. Chem., Int. Ed.* **2006**, *45*, 2897−2901.
(30) Li, L.; Larsen, A. H.; Romero, N. A.; Morozov, V. A.; Glinsvad, C.; Abild-Pedersen, F.; Greeley, J.; Jacobsen, K. W.; Nørskov, J. K. *J. Phys. Chem. Lett.* **2013**, *4*, 222−226.
(31) Qi, L.; Li, J. *J. Catal.* **2012**, *295*, 59−69.
(32) Zhang, S.; Guo, S.; Zhu, H.; Su, D.; Sun, S. *J. Am. Chem. Soc.* **2012**, *134*, 5060−5063.
(33) Chen, H.; Wang, D.; Yu, Y.; Newton, K. A.; Muller, D. A.; Abruña, H. D.; DiSalvo, F. J. *J. Am. Chem. Soc.* **2012**, *134*, 18453−18459.
(34) Wang, D.; Xin, H. L.; Hovden, R.; Wang, H.; Yu, Y.; Muller, D. A.; DiSalvo, F. J.; Abruña, H. D. *Nat. Mater.* **2013**, *12*, 81−87.
(35) Prabhudev, S.; Bugnet, M.; Bock, C.; Botton, G. A. *ACS Nano* **2013**, *7*, 6103−6110.
(36) Sun, S.; Murray, C. B.; Weller, D.; Folks, L.; Moser, A. *Science* **2000**, *287*, 1989−1992.
(37) Sun, S. *Adv. Mater.* **2006**, *18*, 393−403.
(38) Kim, J.; Rong, C.; Liu, J. P.; Sun, S. *Adv. Mater.* **2009**, *21*, 906−909.
(39) Zhang, S.; Onder, M.; Su, D.; Sun, S. *Angew. Chem., Int. Ed.* **2013**, *52*, 3681−3684.
(40) Crewe, A. V.; Wall, J.; Langmore, J. *Science* **1970**, *168*, 1338−1340.
(41) Guo, S.; Zhang, S.; Su, D.; Sun, S. *J. Am. Chem. Soc.* **2013**, *135*, 13879−13884.
(42) Zhang, X.; Lu, G.; Curtin, W. A. *Phys. Rev. B* **2013**, *87*, 054113−054122.
(43) Froemming, N. S.; Henkelman, G. *J. Chem. Phys.* **2009**, *131*, 234103−234109.
(44) Zhang, X.; Lu, G. *J. Phys. Chem. Lett.* **2014**, *5*, 292−297.
(45) Tang, W.; Henkelman, G. *J. Chem. Phys.* **2009**, *130*, 194504−194509.
(46) Kai, T.; Maeda, T.; Kikitsu, A.; Akiyama, J.; Nagase, T.; Kishi, T. *J. Appl. Phys.* **2004**, *95*, 609−612.
(47) Takahashi, Y. K.; Ohnuma, M.; Hono, K. *J. Magn. Magn. Mater.* **2002**, *246*, 259−265.
(48) Sun, X. C.; Kang, S.; Harrell, J. W.; Nikles, D. E.; Dai, Z. R.; Li, J.; Wang, Z. L. *J. Appl. Phys.* **2003**, *93*, 7337−7339.
(49) Gilbert, D. A.; Wang, L. W.; Klemmer, T. J.; Thiele, J. U.; Lai, C. H.; Liu, K. *Appl. Phys. Lett.* **2013**, *102*, 132406−132409.